

An interleaved porous laminate composed of reduced graphene oxide sheets and carbon black spacers by *in situ* electrophoretic deposition†

Cite this: *RSC Adv.*, 2014, 4, 3284Mei Wang,^a Joonsuk Oh,^b Titisa Ghosh,^a Seungchul Hong,^b Giyong Nam,^b Taeseon Hwang^b and Jae-Do Nam^{*ab}

Although the graphene-based materials have a great potential to be used for various energy storage devices, the expected performance of graphene has not been achieved yet seemingly due to the lack of interconnected porosity and actively-exposed surface area that should be developed in the re-stacked graphene electrodes. Herein we used an electrophoretic deposition (EPD) method to fabricate a binder-free porous supercapacitor electrode composed of reduced graphene oxide (RGO) sheets and conductive carbon black (CB) particles. Applying EPD for an electrostatically-stabilized aqueous mixture of RGO and CB nanoparticles, the electrophoretic squeezing force in EPD induced the RGO sheets to align in the in-plane direction along with the CB particles placed in the interlayers of RGO. The developed ladder-like interleaved composite structure allowed a desirable porosity network and conductive path for a facile movement of ions and electrons. Controlling the ratios of concentrations ($C_{s,RGO}/C_{s,CB}$) and/or zeta potentials (ξ_{RGO}/ξ_{CB}) of the RGO and CB nanoparticles in aqueous mixtures, different nanostructures of the interleaved RGO/CB laminates could be fabricated. Thoroughly tested as a supercapacitor electrode in an organic electrolyte (TEA BF₄), the developed RGO/CB electrodes provided excellent performance of the specific capacitance of 218 F g⁻¹ at a scan rate of 1 mV s⁻¹ (133.3 F g⁻¹ at a current density of 2 A g⁻¹), energy density of 43.6 W h kg⁻¹ and power density of 71.3 kW kg⁻¹. It is believed that an ideal performance of intrinsic graphene properties could be exerted by the unique nanostructure of binder-free interleaved graphene laminates as developed by the scalable *in situ* EPD process for large-volume production.

Received 21st October 2013
Accepted 29th November 2013

DOI: 10.1039/c3ra45979a

www.rsc.org/advances

Introduction

Graphene is believed to be an ideal carbon electrode material for various electrochemical energy storage devices like electrical double layer capacitors (EDLCs) because it has large surface area and excellent electrical conductivity.^{1–11} Graphene has been tested as a supercapacitor electrode material usually mixed with other carbon materials,^{12,13} conducting polymers,^{14,15} or transition metal oxides.¹⁶ However, practical application of graphene still faces challenges mostly in the steps of electrode fabrication, where the graphene-sheet mixture are prepared in the liquid media and subsequently re-assembled as a solid-state electrode membrane. In this preparation step, an appropriate nanoscale structure should be developed for accommodating ions and electrons to the active surface of graphene sheets. It is

believed that the exposed surface area and the well-connected open porosity of the re-stacked graphene sheets should be ensured to achieve excellent performance and long-term durability of EDLC.^{7,12–15,17}

More specifically, the graphene-based materials such as graphene oxide (GO) and reduced graphene oxide (RGO) sheets have a strong tendency to restack themselves very densely during drying processing due to the large surface area and the strong van der Waals' force. If this spontaneous and compact restacking of RGO sheets occurs, the desired supercapacitor performance may not be exerted although the intrinsic surface area of graphene-based materials is large.¹³ For supercapacitor electrodes, the interconnected pore network should be guaranteed for ions and electrolytes to move in a facile way. In this sense, conductive particles have been incorporated as a spacer in the restacked graphene layers and tested as supercapacitor electrodes for the purpose of providing porosity.^{12,16} In this approach, the compact restacking of graphene sheets was likely interrupted by the incorporated conductive particles. However, the binder materials (or adhesive glues) were inevitably used in those paste-coating methods and they might very well cover the RGO surface and/or block the open porosity network. We

^aDepartment of Energy Science, Sungkyunkwan University, Suwon, South Korea.
E-mail: jdnam@skku.edu; Fax: +82-31-292-8790; Tel: +82-31-290-7285

^bDepartment of Polymer Science and Engineering, Sungkyunkwan University, Suwon, South Korea

† Electronic supplementary information (ESI) available: XPS spectra of GO and CB, CV curves of RGO and RGO/CB electrodes. See DOI: 10.1039/c3ra45979a

believe that the ideal supercapacitor performance of the graphene-based materials may be achieved by a nanoscale architecturing of the binder-free pore network using, *e.g.*, conductive spacers and graphene sheets.

Various fabrication techniques have been reported for the preparation of binder-free graphene-based membranes, for example, membrane filtration,¹⁸ spin coating,¹⁹ layer-by-layer electrostatic self-assembly,¹² and spray-coating.²⁰ Among these methods, the electrophoretic deposition (EPD) method is an attractive process due to such advantages as high deposition/production rates, excellent purity control, wide-range thickness adjustment, *etc.* For a successful application of EPD on graphene-based materials, a stable aqueous solution is one of the key issues. Recently, our group successfully prepared a stable aqueous suspension of RGO by controlling the reduction rates of graphene sheets and RGO surface charges.¹⁸ Using this stable RGO aqueous suspension, the strong electrophoretic squeezing force in EPD could facilitate cohesive flocculation of RGO sheets desirably to allow no use of binders. Furthermore, when EPD is applied for the mixture of RGO sheets and CB particles, it may well facilitate an alignment of RGO along with CB particles in the in-plane direction and, consequently, an interleaved composite laminate structure could be obtained. This interleaved porous laminate is most likely to provide high electrical- and ionic-conducting paths as required for supercapacitor electrodes.

RGO films have been fabricated by EPD method.^{21–25} However, those studies have suffered from the limited capacitance, for example, 87 F g^{−1} for RGO/carbon nanotubes (CNT) (1 M KCl),²³ 164 F g^{−1} for RGO (6 M KOH),²⁶ 156 F g^{−1} for RGO (0.1 M Na₂SO₄),²⁷ and 151.0 F g^{−1} for RGO/CNT (1.0 M H₂SO₄).²⁸ It is conjectured that appropriate pore networks were not developed in those EPD approaches, seemingly because the

RGO sheets were tightly restacked during EPD. Accordingly, we believe that spacer particles should be adopted in the EPD process of graphene sheets in order to develop open pore networks in the interleaved structure allowing a facile movement of the electrolyte ions. When two heterogeneous entities of graphene sheets and spacer particles are deposited by EPD, it is considered that the relative quantities of RGO and CB should be controlled to achieve a desired interleaved porous structure appropriate for supercapacitor electrode application.

In this study, we developed an *in situ* EPD process to fabricate a binder-free interleaved RGO/CB membrane for supercapacitor electrode application. The electrostatic surface charges of RGO sheets and CB particles were controlled to ensure a stable aqueous mixture of RGO and CB and to give an appropriate interleaved RGO/CB structure. The as prepared RGO/CB electrode was tested in an organic electrolyte supercapacitor, exerting markedly high specific capacitance, as well as high energy and power density.

Results and discussion

Fig. 1a shows a schematic representation of the EPD method. The negative charges of GO and RGO stem from the oxygen-containing function groups,²⁹ and CB from the SO₃^{2−} groups in SDBS. When the voltage is applied to the stainless steel current collector, the negatively charged RGO layers and CB particles move to the positive electrode simultaneously and stick tightly to the surface of stainless steel, giving the interleaved RGO/CB structure. The electric field force makes the GO and RGO sheets stack in the in-plane direction. It is worth noting that we use much lower voltages at 6–8 V than the commonly-used voltages of 30–160 V in most EPD processes.^{22,23,26,27} In those high-voltage EPD processes, various electrochemical redox reactions may

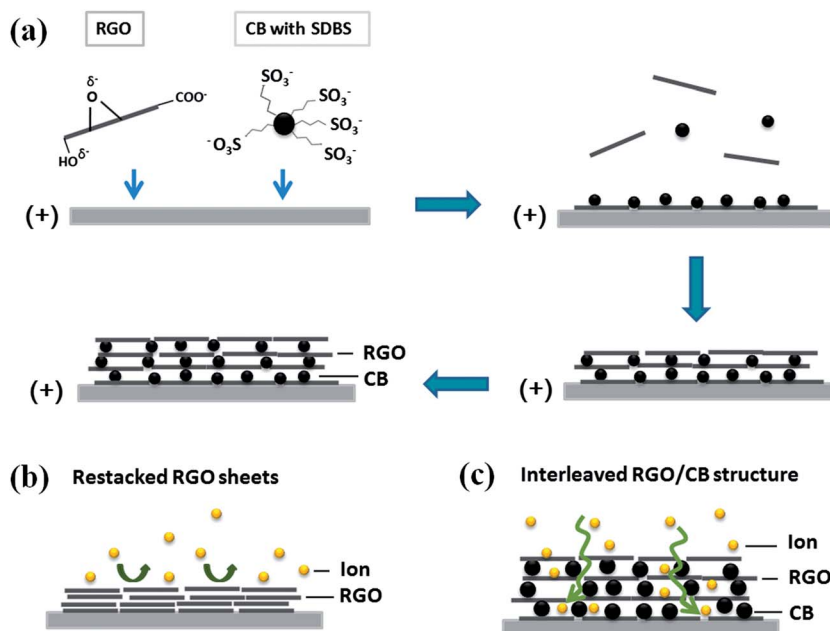


Fig. 1 Representation of the EPD method. Schematic representation of the EPD procedures of interleaved RGO/CB film (a), and schematic representation of the deposited RGO (b) and RGO/CB (c) and the electrolyte ion routes passing through the electrode.

well occur and, thus, bubbles are usually generated on the electrode surfaces heavily, which makes it nearly impossible for the RGO sheets and CB particles to stack in the in-plane direction as an interleaved form with uniformity. Comparing schematically the hypothetical morphology of RGO and RGO/CB layers deposited by EPD in Fig. 1b, the RGO layer by EPD may well become tightly packed due to the electrophoretic force, seemingly indicating that the electrolyte ions hardly permeate into the inner part of RGO layers, which may lead to the incomplete electrochemical utilization of the RGO sheet surface.³⁰ On the other hand, the RGO/CB electrode incorporates the CB particles inside the RGO sheets as spacers, so that the interlayer distance of RGO/CB can adequately accommodate the electrolyte ions.

Fig. 2 shows the cross-sectional images of GO (Fig. 2a), RGO (Fig. 2b), and RGO/CB (Fig. 2c, d and S1†) layers fabricated by the EPD process. It demonstrates that the electric field force makes the GO and RGO layers stacked in the in-plane direction as a layer-by-layer structure. Fig. 2a and b present the slightly-corrugated packing layers of the deposited GO and RGO with thicknesses of 1.06 μm (8 V, 10 min) and 0.556 μm (6 V, 10 min), respectively. In the RGO/CB membrane, it clearly shows that the carbon black particles are located in the RGO interlayer space resultantly to give an interleaved feature with an expanded thickness of 3.39 μm (6 V, 10 min). Comparing the GO (Fig. 2a inset), RGO (Fig. 2b inset), and RGO/CB laminate (Fig. 2c inset), the RGO film exhibits a smooth and glossy surface, indicating that the RGO layers are packed very tightly, while the GO and RGO/CB films are matte. The colour of the GO layers change from dark gray (Fig. 2a inset) to metallic gray (Fig. 2b inset) after the chemical reduction, which is due to the restoration of the sp^2 carbon structures from the oxidized groups.

Fig. 3 presents the zeta-potentials of the GO, RGO and CB suspensions plotted as a function of pH (CB suspension is stabilized by using sodium dodecylbenzenesulfonate, SDBS). In general, when the particles in the colloid have a large negative or positive zeta potential, they repel each other and have no tendency to flocculate. In contrast, when the particles take low zeta potential, there is little repulsive force among the particles, leading to agglomeration.³¹ The pH value of the colloid usually affects the zeta potential of the colloidal particles. The colloid is considered to be stable in the zeta potential range more positive than +30 mV or more negative than -30 mV. Accordingly, as seen in the Fig. 3, all the GO, RGO and CB suspensions would be stabilized when the zeta potential values become ≤ -30 mV in the pH range of 9–10, thus enabling their use for EPD. It is clear that all the GO, RGO and CB colloidal particles take negative charges in the suspension, which would move to the anode in the EPD process simultaneously. Importantly, the RGO and CB should be adjusted at high negative zeta potentials by increasing pH, which ensures a facile deposition of RGO sheets and CB particles under the applied voltage. At pH = 10, the zeta potentials of RGO and CB are 47.7 and 51.1 mV, respectively.

In the EPD process, the deposited mass per unit area m (g cm^{-2}) has been expressed as follows:^{32,33}

$$m = \frac{aC_s\varepsilon_0\varepsilon_r\xi SEt}{\eta} \quad (1)$$

where a is the adhesion factor, C_s is the suspension concentration (g cm^{-3}), ε_0 and ε_r are the permittivity of the free space and the suspension medium, respectively, ξ is the zeta potential of colloidal particles, S is the deposition area (cm^2), E is the electric field (V cm^{-1}), t is time (s), and η is the viscosity of the suspension medium. It indicates that the EPD membrane

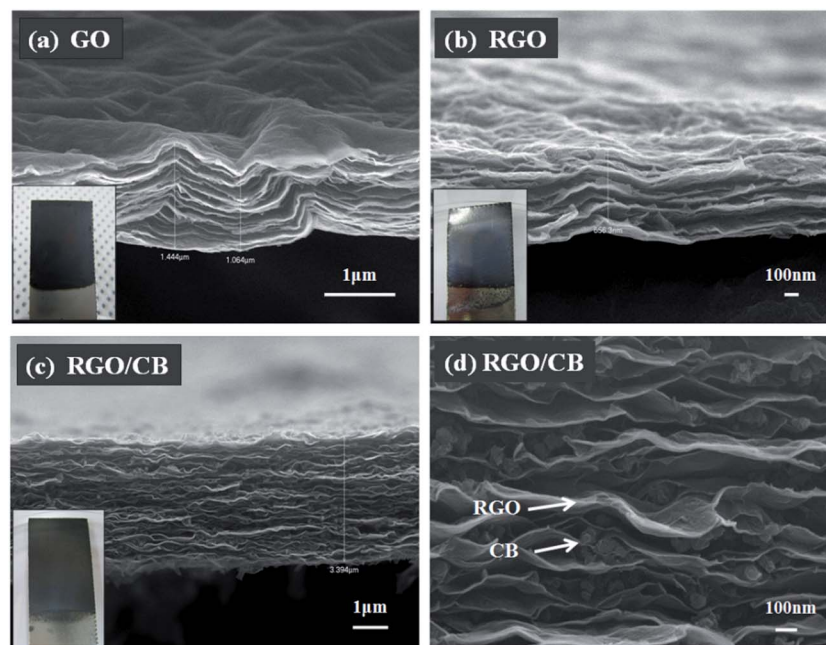


Fig. 2 Cross-sectional FE-SEM images of deposited GO (a), RGO (b), RGO/CB (c and d), and Digital camera images of deposited GO, RGO and RGO/CB membrane on stainless steel substrate (insets of a–c).

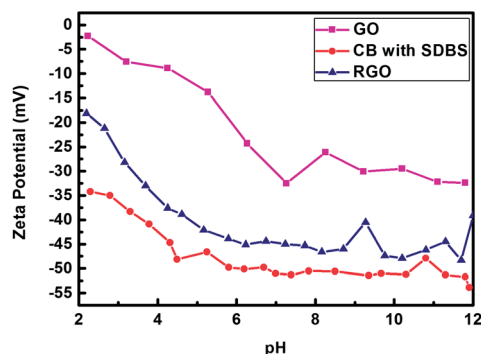


Fig. 3 Zeta Potential of GO, RGO and CB colloid systems as a function of pH. SDBS was added to the CB colloid system.

thickness can be easily changed from several hundred nanometres to a few micrometers by varying the deposition conditions: the concentration of RGO and CB in the suspension, pH of the dispersion (or zeta potential), applied voltage, and deposition time. Simply assuming $a_{\text{RGO}} \approx a_{\text{CB}}$, the weight ratio of RGO to CB in EPD may be estimated as follows:

$$\frac{m_{\text{RGO}}}{m_{\text{CB}}} = \frac{C_{\text{s,RGO}} \xi_{\text{RGO}}}{C_{\text{s,CB}} \xi_{\text{CB}}} \quad (2)$$

Applying the above equation for our experimental composition ($C_{\text{s,RGO}}/C_{\text{s,CB}} = 9$) and zeta potentials ($\xi_{\text{RGO}}/\xi_{\text{CB}} = 0.93$) in Fig. 3, the weight ratio of EPD is evaluated as $m_{\text{RGO}}/m_{\text{CB}} = 8.4$ in the RGO/CB composite membrane. Since the zeta potential of RGO is lower than CB, it is conjectured that the

RGO ratio in the RGO/CB deposition would be lower than that in the initial RGO/CB suspension. Furthermore, since the ratio of the zeta potentials is adjustable by pH of the dispersion media, the relative amount of the RGO and CB in the deposition may be adjusted by the suspension concentration and pH.

The high-resolution C 1s and O 1s spectra of the deposited RGO and RGO/CB films are shown in Fig. 4a and b, respectively. Comparing the spectra of RGO (Fig. 4a) and GO (Fig. S2a†), the peak intensity of oxygen in RGO decreases by the reduction, giving the atomic O/C ratios of GO and RGO as 0.316 and 0.198, respectively (Table 1). It is worth noting that the peak intensity of pi-electron conjugated system in RGO (290.1 eV) is higher than the intensity in GO (290.9 eV), which also indicates the reduction of GO.³⁴ As Fig. S2b† and Table 1 show, the carbon content of RGO/CB (84.58%) is higher than that of RGO (81.22%), since the carbon content of CB is 89.32%, which is higher than 81.22% for RGO. The insets in Fig. 4a (RGO), 4b (RGO/CB), and S2a† (GO) show two prominent deconvoluted components arising from the C-C/C=C bonds at 284.6 eV, C-O

Table 1 Atomic composition list of GO, RGO, CB and RGO/CB after EPD process

Sample name	C (atomic %)	O (atomic %)	N (atomic %)	O/C ratio
GO	75.969	24.031	—	0.316
RGO	81.219	16.110	2.67	0.198
CB	89.323	10.677	—	0.120
RGO/CB	84.582	13.620	1.798	0.161

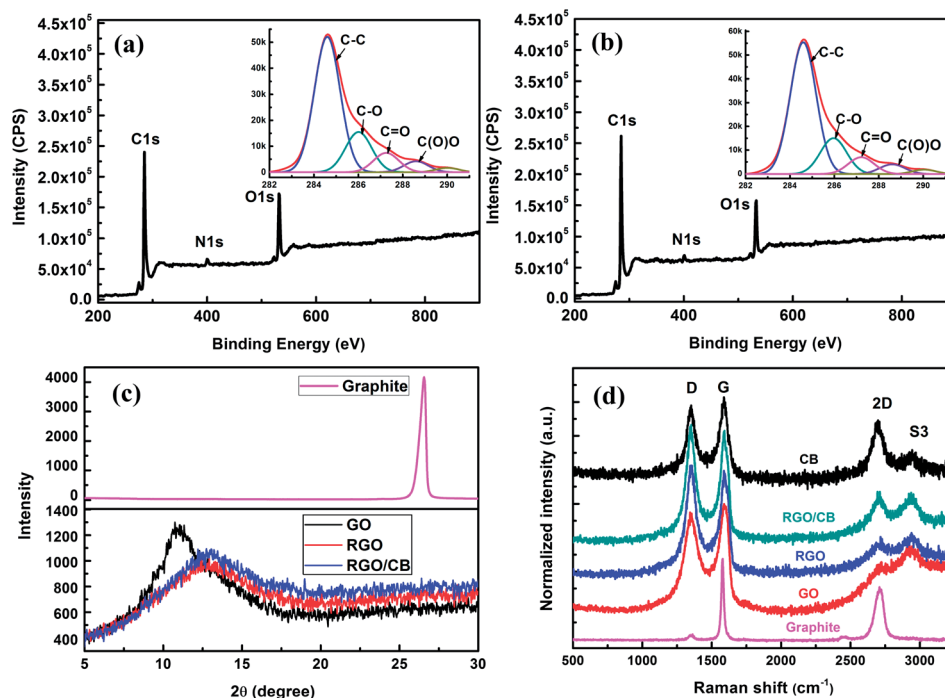


Fig. 4 X-ray photoelectron spectroscopy (XPS) data of RGO (a) and RGO/CB (b). Narrow scan spectra are also included in the insets of (a) and (b). X-ray diffraction (XRD) spectroscopy data of graphite flake, compared with GO, RGO, and RGO/CB membranes prepared by EPD (c), and Raman spectra of graphite flake, electrophoretic deposited GO, RGO, CB, and RGO/CB membranes at an excitation wavelength of 514 nm (d).

(hydroxyl and epoxy) bonds at 286.0 eV and C=O bonds at 287.2 eV. After the reduction process of GO (Fig. S2a† inset), the intensity of the C–O bond decreases (Fig. 4a), while that of the C–C/C=C component increases. This demonstrates that oxygen atoms in GO are partially removed by reduction, and the sp^2 carbon sites are simultaneously restored by reduction. In addition, it should be addressed that there are still oxygen-containing function groups remaining in the RGO (Fig. 4a), which necessarily allows the RGO sheets to be dispersed in water for the following EPD process to be accomplished without using any dispersing agents.¹⁸

Fig. 4c shows high-resolution X-ray diffraction (XRD) spectra of pristine graphite, deposited GO, RGO, and RGO/CB membranes. Comparing the graphite and GO specimens in XRD, the characteristic peak of the pristine graphite at $2\theta = 26.56^\circ$ (d -spacing ≈ 3.36 Å) shifts to $2\theta = 10.96^\circ$ (d -spacing ≈ 8.07 Å) in GO due to the formation of oxygen-containing functional groups during the oxidation. This peak shifts to 13.29° (d -spacing ≈ 6.66 Å) in both RGO and RGO/CB membranes, which is attributed to the removal of the oxygen-containing functional groups. The interlayer space of RGO sheets is larger than that of typical graphene layers in graphite, since RGO needs more interlayer space to accommodate the remaining oxygen-containing functional groups and the water molecules that are trapped in those interlamellar layers. This confirms the successful slightly reduction from GO to RGO with this method, ensuring the EPD fabrication process. Fig. 4d compares the Raman spectra of GO, RGO, CB and RGO/CB membranes prepared by the EPD method. A prominent D-band at 1340 cm^{-1} and G-band at 1580 cm^{-1} are presented in the spectra of the graphite, which coincides with the literature.¹⁸ After the sequential processes of oxidation, exfoliation, and EPD, the D-band intensity of as-prepared GO substantially increases due to the sp^3 hybridization of carbon atoms. As compared with the graphite flake, the G-band of graphite shifts from 1579 cm^{-1} to 1595 cm^{-1} in GO, which is due to the electron withdrawing ability of oxygen-containing functional groups in GO leading to charge transfer from graphene carbon bonds to oxygen-containing functional groups. It is further supported by our experiments that the G-band position of RGO shifts from 1595 cm^{-1} (GO) to 1590 cm^{-1} due to the removal of oxygen functional groups by chemical reduction of GO.^{35,36}

As shown in Fig. 5a, the cyclic voltammetry (CV) measurements of RGO and RGO/CB membranes in an organic electrolyte of TEA BF_4 exhibit a quasi-rectangular shape superimposed with a pair of Faradaic peaks, indicating the coexistence of an EDL capacitance and pseudocapacitance. The pseudocapacitance is believed to originate from the reactions of functional groups, where the electrons are stored and released during the cyclic voltammetric measurement.³⁷ The Faradaic peaks of RGO/CB are higher than that of RGO, which is because that the insertion of CB increases the interlayer distance of RGO, thus, more oxygen-containing functional groups can contact with the electrolyte. It can be seen that the current density of RGO/CB is higher than that of RGO, which indicates the capacitance of RGO/CB would be higher than that of RGO (Fig. 5a and S3†). The CV curves of the RGO/CB electrode are shown in Fig. 5b at

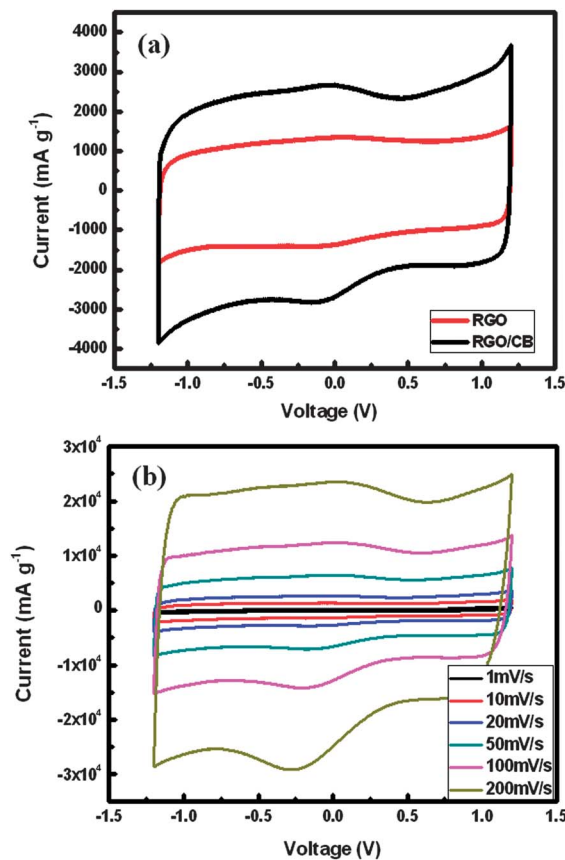


Fig. 5 Cyclic Voltammetry measurement of RGO and RGO/CB membrane electrodes in the scan rate of 20 mV s^{-1} (a), and RGO/CB membrane electrode in scan rates of 1, 10, 20, 50, 100, and 200 mV s^{-1} (b).

various scan rates ranging from 1 to 200 mV s^{-1} (see the CV curves of RGO electrode in Fig. S4†). The CV curve of the RGO/CB composite laminate maintains quasi-rectangular shape superimposed with a pair of Faradaic peaks even at a high scan rate of 200 mV s^{-1} , which indicates that the EDLC charge-discharge process is desirably ensured at such high speeds seemingly due to the unique morphology of our RGO/CB composite laminates. It is believed that a low contact resistance of the RGO/CB particles and fast diffusion rates of electrolyte ions are achieved in the supercapacitor electrodes.^{13,38}

Using the CV results, the specific capacitance can be evaluated by the following equation:

$$C(\nu) = \frac{I\Delta t}{m\Delta V} = \frac{\Delta t}{2m\Delta V} [I_a(\nu) + I_c(\nu)] = \frac{1}{2m\nu} [I_a(\nu) + I_c(\nu)] \quad (3)$$

where $I_a(\nu)$ and $I_c(\nu)$ are the average anodic and cathodic current in one cycle of potential sweep, m is the weight of as-deposited electrode material, ΔV is the potential range, and ν is the scan rate. As shown in Fig. 5b and S5,† the capacitances of RGO and RGO/CB evaluated by eqn (3) are 71.4 F g^{-1} (0.0068 F cm^{-2}) and 138.4 F g^{-1} (0.0175 F cm^{-2}), respectively, at the scan rate of 10 mV s^{-1} . The specific capacitance of RGO in this study is measured as 71.4 F g^{-1} , which is similar to other reported values of $40\text{--}60\text{ F g}^{-1}$ (activated carbon), $20\text{--}80\text{ F g}^{-1}$ (carbon

nanotubes), and 82–99 F g⁻¹ (graphene) in organic electrolyte.^{7,39,40} However, the capacitance of the developed RGO/CB supercapacitor is 138.4 F g⁻¹, which is much higher than that of the RGO in this study. In the RGO/CB system, it confirms that the CB particles play an important role as spacers, increasing the interlayer distance of the RGO sheets and subsequently allowing the RGO surfaces to be readily accessible to the electrolyte and ions. On the other hand, the RGO sheets restack themselves tightly in the EPD and drying process, leaving no space for the ions to move.

The specific capacitance values of RGO/CB at different potential scan rates are shown in Fig. 6a. Impressively, the

specific capacitance of the RGO/CB electrode reaches as high as 218.0 F g⁻¹ (0.0276 F cm⁻²) in a low scan rate of 1 mV s⁻¹, which is excellent in organic-electrolyte EDLC systems and could possibly allow large-area mass-production supercapacitor applications. The capacitance value decreases with the increment of scan rate, but it reaches 98.8 F g⁻¹ (0.0125 F cm⁻²) at a high scan rate of 1000 mV s⁻¹, which is also substantially high as compared with reported literature values. For example, a supercapacitor electrode of chemically modified graphene was reported to provide 99 F g⁻¹ (scan rate 20 mV s⁻¹) in TEA BF₄ electrolyte,⁹ which is much lower than our RGO/CB electrode value of 136 F g⁻¹ measured at the same scan rate. It is important to note that a RGO/CB electrode fabricated by filtration was reported to give 83.2 F g⁻¹ (scan rate 10 mV s⁻¹) in organic electrolyte,⁴¹ which is 40% lower than our capacitance.

Galvanostatic charge–discharges also conducted to evaluate the capacitances of the RGO/CB and RGO supercapacitors. As shown in Fig. 6b, the discharge time of RGO/CB is much longer than that of RGO, indicating much higher capacitance of RGO/CB than RGO. Calculated by eqn (3), the specific capacitance of RGO/CB and RGO are 133.3 F g⁻¹ and 75.0 F g⁻¹, respectively. Impressively, the IR drop of RGO/CB is obviously lower than that of RGO, as presented in the inset of Fig. 6b. These results indicate that the CB particles in the interlayers of interleaved RGO efficiently increase the capacitance and conductivity of the RGO sheets. In addition, the cycle ability of RGO/CB is also evaluated by repeating the CV test at a scan rate of 200 mV s⁻¹ and galvanostatic charge–discharge measurement at a current density of 10 A g⁻¹ for 1000 cycles in TEA BF₄ organic electrolyte. The specific capacitance of RGO/CB as a function of cycle number is shown in Fig. 6c. During the galvanostatic charge–discharge measurement, no capacitance degradation appears in the RGO/CB coin cell within 1000 cycles, indicating a very stable electrode material. While in the CV measurement, RGO/CB electrode shows 90.5% capacitance retention at the 1000th cycle, which may result from the moisture in the air, poisoning the performance of TEA BF₄ electrolyte.

The specific energy and specific power can be evaluated to give the Ragone plot as follows:⁴²

$$E = \frac{C(\nu)\Delta V^2}{8}, P = \frac{E}{\Delta t(\nu)} = \frac{E\nu}{\Delta V} \quad (4)$$

where $\Delta t(\nu)$ is the time for anodic or cathodic potential sweep in different scan rates. As shown in Fig. 7, the highest energy density of 43.6 W h kg⁻¹ (with power density of 157.0 W kg⁻¹) and the highest power density of 71.3 kW kg⁻¹ (with energy density of 19.8 W h kg⁻¹) are obtained at the scan rates of 1 mV s⁻¹ and 1000 mV s⁻¹, respectively. Compared with literature values of graphene-based EDLC in organic electrolyte, for example, 26 W h kg⁻¹ in organic electrolyte,⁴¹ our RGO/CB supercapacitor shows superior performance of energy and power densities, indicating that the intrinsic capabilities of graphene-based materials are successfully exerted in supercapacitor performance.

The supercapacitor performance of the RGO and RGO/CB electrodes is further investigated by the Nyquist plots (Fig. 8a).

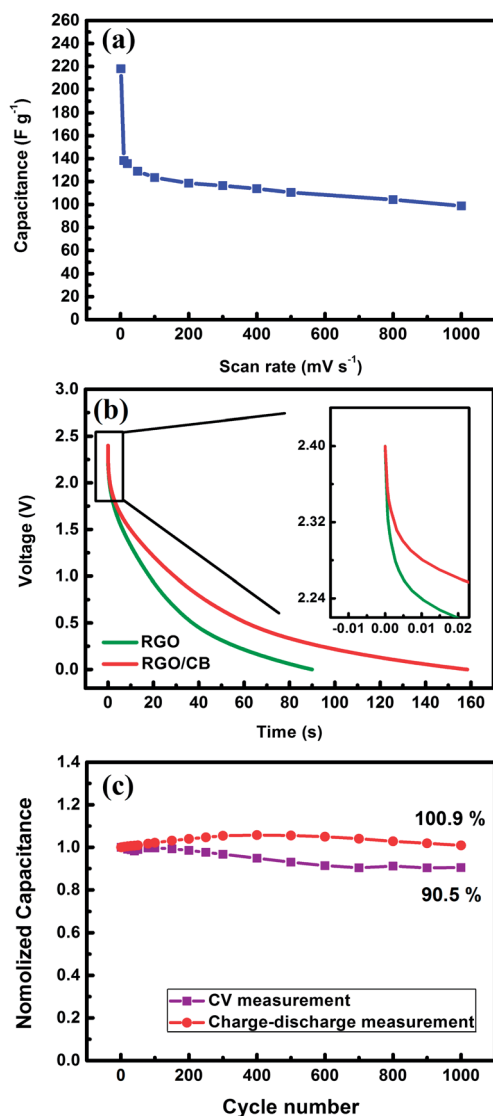


Fig. 6 Specific capacitance of RGO/CB at different potential scan rates (a). Discharge curves of RGO and RGO/CB coin cells measured by galvanostatic charge–discharge at current density of 2 A g⁻¹ (b), with the IR drop details in the inset. Cycle ability of RGO/CB measured at the scan rate of 200 mV s⁻¹ by CV measurement and the current density of 10 A g⁻¹ by charge–discharge measurement in TEA BF₄ electrolyte (c).

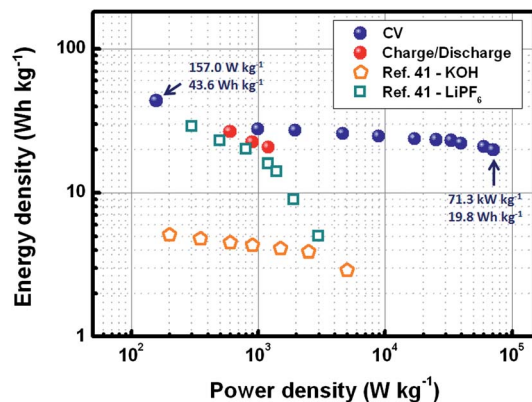


Fig. 7 Ragone plot of RGO/CB electrode measured by CV and galvanostatic charge–discharge measurement and the Ragone plot from ref. 41.

The RGO/CB gives a linear shape in the low-frequency region and an inconspicuous loop in the high-frequency region, showing good electrode contact. The impedance curve intersects the x -axis at a 45° angle, which is the typical feature of a porous electrode saturated with electrolyte.⁴³ As seen in the inset of Fig. 8a(A), the equivalent series resistances (ESR) of RGO and RGO/CB, as obtained from x -intercept of the Nyquist plots, are $13.3\ \Omega$ and $6.0\ \Omega$ in the TEA BF_4 electrolyte, respectively. These values correspond to the $|Z|$ values in the

high-frequency region ($\sim 10^5\ \text{Hz}$) in Fig. 8b. In this region ($>1\ \text{kHz}$), the Bode $|Z|$ includes the resistance of the electrolyte and electrode materials.⁴⁴ When the RGO/CB electrode is measured in the $1\ \text{M}\ \text{H}_2\text{SO}_4$ electrolyte, the ESR of RGO/CB ($0.3\ \Omega$, as shown in Fig. 8a(B)) is much smaller than that of RGO/CB in TEA BF_4 electrolyte due to the large resistance of organic electrolyte. The low ESR value of RGO/CB electrolyte in H_2SO_4 electrolyte also indicates the low internal resistance of RGO/CB electrode material. As shown in Fig. 8b, at the frequency of $10^5\ \text{Hz}$, the $|Z|$ of RGO/CB is much smaller than that of the RGO electrode, giving $13.3\ \Omega$ for RGO and $6.0\ \Omega$ for RGO/CB, which is supported by the values obtained from Nyquist plots. This demonstrates that the resistance of RGO/CB is much smaller than that of RGO. The phase angle as a function of frequency is also shown in Fig. 8b. At high frequency ($\sim 10^5\ \text{Hz}$), the phase angles for both supercapacitors are almost zero, which is usually observed in EDLC systems. When the frequency decreases, the phase angle increases. The phase angles are 83° for RGO and 79° for RGO/CB at $7\ \text{mHz}$, indicating that our RGO/CB supercapacitor is close to an ideal capacitor (phase angle at 90°).⁴⁵ In our RGO/CB system, the inserted CB particles facilitate electron transfer through the stacked RGO sheets, giving decreased electrical resistance, and substantially high capacitance and power density.

We believe that the in-plane alignment and through-thickness consolidation of the RGO/CB sheets are keys for the fabrication of a highly conductive electrode. Our study clearly indicates that the insertion of CB among the RGO layers increases the interlayer spacing of RGO, and thus facilitates the mobility of ions as well as electrons to give substantially high supercapacitor performance. Furthermore, since the RGO sheets and CB particles are driven by the electrical field, they are deposited on the current collector in a uniform and compact manner, providing low contact impedance at the interface of the electrode materials and current collector. The interleaved RGO/CB also provides a conductive network in an effective way through the sheet plane, which substantially decreases the ESR of the electrode.

Experimental

Materials preparation

Graphite oxide was prepared by the oxidation of graphite (Sigma-Aldrich) in the modified Hummers method.^{46,47} $0.3\ \text{g}$ of graphite oxide was dispersed in $200\ \text{mL}$ of DI water with ultrasonication for $4\ \text{h}$, followed by centrifugation at $4000\ \text{rpm}$ for $15\ \text{min}$ to remove the unexfoliated graphite oxide flakes. The prepared GO solution ($1.5\ \text{mg}\ \text{mL}^{-1}$) was reduced by a rate-controlled reduction method to prepare the RGO aqueous suspension.¹⁸ The exfoliated GO suspension was put into an ice bath to cool it down to $0\text{--}5\ ^\circ\text{C}$, followed by the dropwise addition of $5\ \text{mM}$ hydrazine solution ($35\ \text{wt}\%$, Sigma-Aldrich). Subsequently, the suspension was heated on a flat heater at around $200\ ^\circ\text{C}$ for $35\ \text{min}$ for further reduction. Throughout the reduction process, the suspension was mildly stirred with a magnetic bar. The resulting suspension was a RGO suspension with pH $9\text{--}10$.

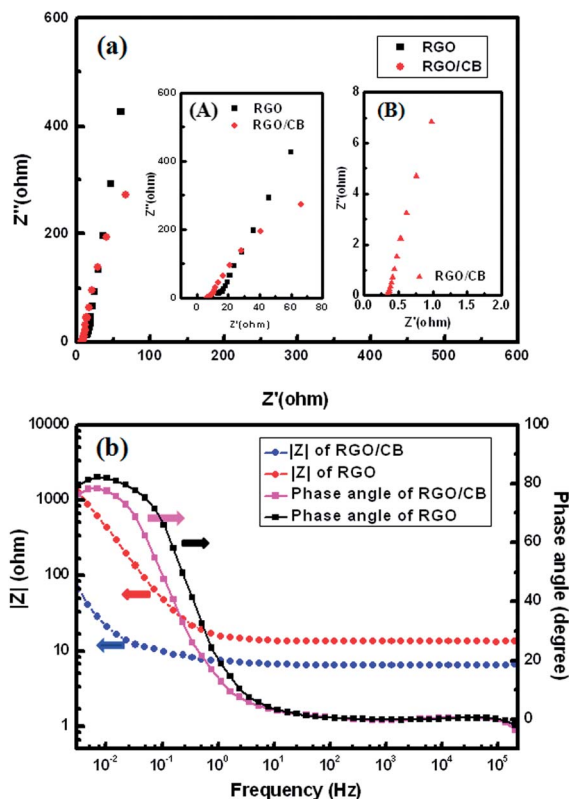


Fig. 8 Nyquist plots of RGO and RGO/CB membrane electrodes (a), and Bode $|Z|$ and Bode angle plots over the frequency range from $200\ \text{kHz}$ to $3\ \text{mHz}$ (b).

The GO aqueous solution (1.5 mg mL^{-1}) was also prepared by the ultra-sonication (4 h) and centrifugation (15 min) of the graphite oxide. Before sonication, the pH of the graphite oxide suspension was adjusted by NaCO_3 to 9–10 to maintain the suspension stability. Carbon black (acetylene black, Alfa Aesar) suspension (1 mg mL^{-1}) was prepared by adding carbon black and SDBS (80 wt%, Sigma-Aldrich) at a weight ratio of 4 : 1 to DI-water and applying ultra-sonication for 4 h. The pH of the obtained CB suspension was adjusted to 9. For preparation of the RGO/CB deposition suspension, the CB suspension was added into the RGO solution, with an RGO/CB weight ratio of 9 : 1.

The EPD of GO, RGO, CB and RGO/CB were all carried out with the aqueous suspension at room temperature. RGO/CB composite films were fabricated by the EPD method, as schematically shown in Fig. 1a. A direct-current (DC) voltage of 6 V was applied to stainless steel electrodes for 10 min, and RGO/CB was deposited on the anode electrode. The detailed EPD conditions and sample descriptions are shown in Table 2. After EPD deposition, samples were washed with DI-water and dried in air at room temperature.

Characterization

The microstructure of the samples was characterized by field emission scanning electron microscopy (FE-SEM, JEOL, JEM 7000F, Japan). The Zeta potentials of GO, RGO and CB were measured by laser Doppler electrophoresis with a Zetasizer Nano-ZS (Malvern Instruments Ltd., Worcestershire, United Kingdom). HCl (0.25 M) and NaOH (0.25 M) were used to adjust the pH. X-ray photoelectron spectroscopy (XPS, QUANTUM 2000, Physical electronics, USA) was performed using focused monochromatized Al $K\alpha$ radiation ($h\nu = 1486.6 \text{ eV}$), which was corrected by the C 1s line at 284.6 eV. The interlayer information of samples was obtained by X-ray diffraction (XRD, Bruker, D8 Discover) with $\text{CuK}\alpha$ radiation ($\lambda = 0.154 \text{ nm}$) in the 2θ range of 5 to 40 degrees with a scanning speed of 3° min^{-1} . Raman spectroscopy (Renishaw, RM-1000 Invia) with excitation energy of 2.41 eV and wavelength of 514 nm (Ar^+ ion laser) was used. Cyclic voltammetry, galvanostatic charge–discharge and electrochemical impedance spectroscopy (EIS) was obtained by multichannel potentiostat and galvanostat (Bio-Logic Science Instruments, VMP3). Three-electrode CV was performed in TEA BF_4 electrolyte in a potential window of -1.2 to 1.2 V with different scan rates. The RGO and RGO/CB deposited on the stainless steel substrate were directly used as the working electrode, with Pt as the counter electrode, and an Ag/AgCl electrode as the reference electrode.

Table 2 EPD conditions of GO, RGO, RGO/CB and CB

Sample name	Voltage (V)	Time (min)	Description
GO	8	10	Black
RGO	6	10	Gray, shining
CB	8	10	Black
RGO/CB	6	10	Gray

Conclusions

In this study, we reported a novel one-step method to prepare an interleaved RGO/CB binder-free supercapacitor electrode by the EPD process particularly operated at low voltage. The stability and surface charge of the RGO and CB particles were ensured by the zeta-potential analysis to give an interleaved architecture of graphene/CB composites. The RGO/CB electrode exhibits good supercapacitor properties, with a capacitance of 218 F g^{-1} measured at a scan rate of 1 mV s^{-1} , 133.3 F g^{-1} at a current density of 2 A g^{-1} , and ESR of 6Ω in TEA BF_4 electrolyte (0.3Ω in H_2SO_4 electrolyte). High energy density of 43.6 W h kg^{-1} and power density of 71.3 kW kg^{-1} were obtained from the developed RGO/CB supercapacitor. Our work demonstrated that a binder-free supercapacitor electrode could be fabricated by the graphene-based materials using an *in situ* EPD process. It allowed the ideal performance of intrinsic graphene properties to be exerted in supercapacitors. Further study and optimization of this method will be reported in the future.

Acknowledgements

This research was supported by the WCU (World Class University) program (R31-2008-10029) and the research grants (2010-0028939, 2012-0006672) through the National Research Foundation of Korea funded by the Ministry of Education, Science and Technology. We also appreciate the project and equipment support from Gyeonggi Province through the GRR program at Sungkyunkwan University.

Notes and references

- 1 G. Zhao, T. Wen, C. Chen and X. Wang, *RSC Adv.*, 2012, **2**, 9286.
- 2 M. Zhi, C. Xiang, J. Li, M. Li and N. Wu, *Nanoscale*, 2013, **5**, 72.
- 3 Y. Zhu, S. Murali, M. Stoller, K. Ganesh, W. Cai, P. Ferreira, A. Pirkle, R. Wallace, K. Cychosz, M. Thommes, D. Su, E. Stach and R. Ruoff, *Science*, 2011, **332**, 1537.
- 4 S. Nardecchia, D. Carriazo, M. Ferrer, M. Gutiérrez and F. Monte, *Chem. Soc. Rev.*, 2013, **42**, 794.
- 5 W. Chen, R. Rakhi and H. Alshareef, *Nanoscale*, 2013, **5**, 4134.
- 6 J. Xia, F. Chen, J. Li and N. Tao, *Nat. Nanotechnol.*, 2009, **4**, 505.
- 7 D. Su and R. Schlögl, *ChemSusChem*, 2010, **3**, 136.
- 8 T. Kuila, A. K. Mishra, P. Khanra, N. H. Kim and J. H. Lee, *Nanoscale*, 2013, **5**, 52.
- 9 M. Stoller, S. Park, Y. Zhu, J. An and R. Ruoff, *Nano Lett.*, 2008, **8**, 3498.
- 10 L. L. Zhang, X. Zhao, M. D. Stoller, Y. Zhu, H. Ji, S. Murali, Y. Wu, S. Perales, B. Clevenger and R. S. Ruoff, *Nano Lett.*, 2012, **12**, 1806.
- 11 X. Yang, F. Zhang, L. Zhang, T. Zhang, Y. Huang and Y. Chen, *Adv. Funct. Mater.*, 2013, **23**, 3353.
- 12 D. Yu and L. Dai, *J. Phys. Chem. Lett.*, 2010, **1**, 467.

- 13 J. Yan, T. Wei, B. Shao, F. Ma, Z. Fan, M. Zhang, C. Zheng, Y. Shang, W. Qian and F. Wei, *Carbon*, 2010, **48**, 1731.
- 14 D. Wang, F. Li, J. Zhao, W. Ren, Z. Chen, J. Tan, Z. Wu, I. Gentle, G. Lu and H. Cheng, *ACS Nano*, 2009, **3**, 1745.
- 15 Y. Luo, D. Kong, Y. Jia, J. Luo, Y. Lu, D. Zhang, K. Qiu, C. Li and T. Yu, *RSC Adv.*, 2013, **3**, 5851.
- 16 Z. Wu, D. Wang, W. Ren, J. Zhao, G. Zhou, F. Li and H. Cheng, *Adv. Funct. Mater.*, 2010, **20**, 3595.
- 17 R. Kötz and M. Carlen, *Electrochim. Acta*, 2000, **45**, 2483.
- 18 T. Ghosh, C. Biswas, J. Oh, G. Arabale, T. Hwang, N. Luong, M. Jin, Y. Lee and J. Nam, *Chem. Mater.*, 2012, **24**, 594.
- 19 G. Eda, H. Unalan, N. Rupasinghe, G. Amaratunga and M. Chhowalla, *Appl. Phys. Lett.*, 2008, **92**, 233502.
- 20 V. Pham, T. Cuong, S. Hur, E. Shin, J. Kim, J. Chung and E. Kim, *Carbon*, 2010, **48**, 1945.
- 21 S. Hasan, J. Rigueur, R. Harl, A. Krejci, I. Juan, B. Rogers and J. Dickerson, *ACS Nano*, 2010, **4**, 7367.
- 22 Z. Wu, S. Pei, W. Ren, D. Tang, L. Gao, B. Liu, F. Li, C. Liu and H. Cheng, *Adv. Mater.*, 2009, **21**, 1756.
- 23 T. Lu, L. Pan, H. Li, C. Nie, M. Zhu and Z. Sun, *J. Electroanal. Chem.*, 2011, **661**, 270.
- 24 V. Lee, L. Whittaker, C. Jaye, K. Baroudi, D. Fischer and S. Banerjee, *Chem. Mater.*, 2009, **21**, 3905.
- 25 Z. Niu, J. Du, X. Cao, Y. Sun, W. Zhou, H. H. Hng, J. Ma, X. Chen and S. Xie, *Small*, 2012, **8**(20), 3201.
- 26 Y. Chen, X. Zhang, P. Yu and Y. Ma, *J. Power Sources*, 2010, **195**, 3031.
- 27 S. Liu, J. Ou, J. Wang, X. Liu and S. Yang, *J. Appl. Electrochem.*, 2011, **41**, 881.
- 28 S. Wang and R. A. W. Dryfe, *J. Mater. Chem. A*, 2013, **1**, 5279.
- 29 S. An, Y. Zhu, S. Lee, M. Stoller, T. Emilsson, S. Park, A. Velamakanni, J. An and R. Ruoff, *J. Phys. Chem. Lett.*, 2010, **1**, 1259.
- 30 J. Yoo, K. Balakrishnan, J. Huang, V. Meunier, B. Sumpter, A. Srivastava, M. Conway, A. Reddy, J. Yu, R. Vajtai and P. Ajayan, *Nano Lett.*, 2011, **11**, 1423.
- 31 C. Lee, T. Hwang, G. Nam, J. Hong, D. Lee, J. Oh, S. Kwak, S. Lee, W. Lee, K. Yang, J. Park, Y. Lee, K. Chung, Y. Lee, H. Choi and J. Nam, *Composites, Part A*, 2011, **42**, 1826.
- 32 B. Ferrari and R. Moreno, *J. Eur. Ceram. Soc.*, 2010, **30**, 1069.
- 33 D. Hanaor, M. Michelazzi, P. Veronesi, C. Leonelli, M. Romagnoli and C. Sorrell, *J. Eur. Ceram. Soc.*, 2011, **31**, 1041.
- 34 N. Lachman, X. Sui, T. Bendikov, H. Cohen and H. D. Wagner, *Carbon*, 2012, **50**, 1734.
- 35 M. Jin, H. Jeong, T. Kim, K. So, Y. Cui, W. Yu, E. Ra and Y. Lee, *J. Phys. D: Apply. Phys.*, 2010, **43**, 275402.
- 36 X. Dong, D. Fu, W. Fang, Y. Shi, P. Chen and L. Li, *Small*, 2009, **5**, 1422.
- 37 Y. Fang, B. Luo, Y. Jia, X. Li, B. Wang, Q. Song, F. Kang and L. Zhi, *Adv. Mater.*, 2012, **24**, 6348.
- 38 Y. Wang, Z. Shi, Y. Huang, Y. Ma, C. Wang, M. Chen and Y. Chen, *J. Phys. Chem. C*, 2009, **113**, 13103–13107.
- 39 K. Ku, B. Kim, H. Chung and W. Kim, *Synth. Met.*, 2010, **160**, 2613.
- 40 N. Jung, S. Kwon, D. Lee, D. M. Yoon, Y. M. Park, A. Benayad, J. Y. Choi and J. S. Park, *Adv. Mater.*, 2013, DOI: 10.1002/adma.201302788.
- 41 G. Wang, X. Sun, F. Lu, H. Sun, M. Yu, W. Jiang, C. Liu and J. Lian, *Small*, 2012, **8**, 452.
- 42 J. Jang, A. Kato, K. Machida and K. Naoi, *J. Electrochem. Soc.*, 2006, **153**, A321.
- 43 C. Niu, E. Sichel, R. Hoch, D. Moy and H. Tennent, *Appl. Phys. Lett.*, 1997, **70**, 1480.
- 44 J. Miller and B. Dunn, *Langmuir*, 1999, **15**, 799.
- 45 F. Lufrano and P. Staiti, *Electrochim. Acta*, 2004, **49**, 2683.
- 46 D. Marcano, D. Kosynkin, J. Berlin, A. Sinitskii, Z. Sun, A. Slesarev, L. Alemany, W. Lu and J. Tour, *ACS Nano*, 2010, **4**, 4806.
- 47 J. Oh, T. Hwang, G. Nam, J. Hong, A. Bae, S. Son, G. Lee, H. Sung, H. Choi, J. Koo and J. Nam, *Thin Solid Films*, 2012, **521**, 270.